73rd International Astronautical Congress (IAC), Paris, France, 18-22 September 2022.

IAC-22-A6.9.4

Detection of Satellite Manoeuvres Using Non-Linear Kalman Filters on Passive-Optical Measurements

Christoph Bergmann[a*], Andrea Zollo[a], Johannes Herzog[a], Hauke Fiedler[a], Thomas Schildknecht[b]

[a] *German Aerospace Center, Münchener Straße 20, D-82234 Weßling, Germany, christoph.bergmann@dlr.de*
[b] *Astronomical Institute, University of Bern, Sidlerstr. 5, CH-3012 Bern, Switzerland*
[*] *Corresponding author*

Abstract

As part of an ongoing effort to build and maintain a data base for Space Situational Awareness, we have been developing an algorithm that employs a non-linear Kalman Filter to detect satellite manoeuvres. This methodology works directly on the astrometric angle measurements derived from passive-optical telescope observations without the need to run an orbit determination step first. In this study, we analyze the performance of this algorithm using large data sets of synthetic observations, and use it to detect and characterize several manoeuvres performed by geostationary satellites.

In order to assess the capabilities and limitations of this method, we first created a large set of synthetic observations based on precisely known orbits of Galileo satellites. With that in hand, we study the effects of varying different properties of the data, such as the noise level, manoeuvre magnitude, and manoeuvre direction.

As a second step, we apply the manoeuvre detection algorithm to real astrometric observations of two geostationary satellites obtained with optical telescopes of the SMARTnet sensor network, including observations during the launch and early orbit phase. Like our simulated observations, our real-world data set comprises manoeuvres of very different magnitudes and directions. In some cases, the true manoeuvre details were known to us, so we could verify our findings.

We detect a number of manoeuvres in our observations, and in one case, we also accurately determine the manoeuvre epochs and $\Delta\mathbf{v}$-components. This is done by means of a conjunction analysis, during which we calculate the collision probability between two tracks propagated forward and backward, respectively. We then determine the manoeuvre epoch and $\Delta\mathbf{v}$-components at the time of maximum collision probability. We show that with this method we can determine the manoeuvre epoch to within a few seconds, and the $\Delta\mathbf{v}$-components to an accuracy at the cm/s-level.

1 Introduction

Most active satellites perform station-keeping manoeuvres on a regular basis. In order to maintain a data base containing accurate orbit information of resident space objects successfully, it is imperative to include manoeuvre information. Without knowing about manoeuvres, the orbit accuracy of the data base objects will decrease over time. This can eventually lead to wrong object associations, duplicate entries, and/or the loss of an object from the data base. Therefore, the ability to detect and subsequently characterize satellite manoeuvres automatically plays a pivotal role for the safe and sustainable use of space from a Space Situational Awareness point of view.

Traditional manoeuvre detection methods often look for sudden changes in the time series of orbital elements (e.g. [1, 2]), or the difference between the predicted states and the updated state estimates after adding a new measurement (e.g. [3]). A Linear Kalman filter has also been used to de-

tect inconsistencies in the orbital elements [4]. Another approach is to detect manoeuvres by performing a conjunction analysis and screening the encounter probability between two tracks for maxima [5]. Extended Kalman Filters (EKFs) have also been shown to be useful tools for manoeuvre detection and estimation (e.g. [6]).

We have been developing a manoeuvre detection algorithm based on non-linear Kalman filters [4, 7]. Owing to the sequential nature of the Kalman filter, manoeuvres can quickly be identified by analyzing the filter residuals whenever a new observation is added, without having to re-run an orbit determination (OD) step on the entire historical set of observations. While we have working prototypes for an Unscented Kalman Filter (UKF) and EKF that produce comparable results, we solely focus on the UKF for this study.

We describe our data acquisition and the creation of the synthetic observations in Section 2, followed by a description of the manoeuvre detection and conjunction analysis approaches in Section 3. Results obtained using the synthetic and real observations are presented in Section 4. We then discuss our findings and give a brief outlook in Section 5.

2 Data

2.1 SMARTnet Observations

Observations for this work were carried out using one of our SMARTnet [8] telescope stations (SMART-01-SUTH), located at the South African Astronomical Observatory near Sutherland, South Africa. The station is comprised of two telescopes, a smaller 20-cm telescope, which is mainly used for survey operations, and a larger 50-cm telescope used mainly for follow-up observations.

Typically, these observations are grouped together in series of about 7 single-shot exposures. They are passive-optical observations, each yielding a pair of astrometric angle measurements for right ascension (RA, α) and declination (DEC, δ). Together, all angle measurements within a given series form a tracklet. Astrometric data reduction is automatically performed with the `ZimControl` software package [9].

2.2 Synthetic Observations

For the performance analysis of our manoeuvre detection algorithm, we created numerous data sets of synthetic observations, while varying different properties of the data, namely the noise level, the manoeuvre magnitude, and the manoeuvre direction.

All data sets were based on model orbits obtained by numerically propagating a state vector of a Galileo satellite to the desired observation epochs while taking into account the simulated manoeuvre as well as non-Keplerian perturbations (gravitational force of the non-spherical Earth, gravitational pulls of the Sun and the Moon, and Solar radiation pressure). The resulting state vectors are then transformed into topocentric right ascension and declination, assuming SMART-01-SUTH as the telescope station, before adding white noise to the model. Note that we simulate every manoeuvre as impulsive, meaning the change in velocity happens instantaneously while the position remains unchanged.

3 Methodology

3.1 Manoeuvre Detection

We mainly follow the method described in [7]. That is, we apply a UKF to astrometric angle measurements derived from passive-optical observations[1]. The basic idea is that when adding a new observation, the UKF will be sensitive to any unexpected deviations from the numerically propagated model of the previous state.

The state transition function f is defined by

$$\bar{\mathbf{x}}_k = f(\mathbf{x}_{k-1}) \quad , \tag{1}$$

where $\bar{\mathbf{x}}_k$ is the prior state estimate at step k, and $\mathbf{x}_{k-1}$ is the posterior state after the previous step. We implemented f as a numerical propagation including as non-Keplerian perturbations the full geopotential up to order and degree (20, 20), the gravitational pulls of the Sun and the Moon, and the Solar radiation pressure. Furthermore, we define the measurement function h, which calculates the two-dimensional topocentric model obser-

[1] Here, we focus solely on the UKF, although very similar results can be obtained using the EKF [7].

vations from the six-dimensional prior state estimate, via

$$\mathbf{y}_k = \mathbf{z}_k - h(\bar{\mathbf{x}}_k) \quad , \tag{2}$$

where $\mathbf{y}_k$ and $\mathbf{z}_k$ are the filter residuals and the measurements at time step k, respectively. The implementation of h includes the conversion between the International Terrestrial Reference Frame and the Geocentric Celestial Reference Frame. The UKF was initialized in the same way as explained in [7].

We have tried two quantities as possible manoeuvre indicators. First, we used the squared and normalized residuals in measurement space following [10], defined by

$$\varepsilon = \mathbf{y}^{\mathrm{T}} \, \mathbf{S}^{-1} \, \mathbf{y} \quad . \tag{3}$$

Here, $\mathbf{S}$ is the innovation covariance matrix, that is, the covariance matrix in measurement space. Similarly, we define the squared and normalized residuals in state space by

$$\xi = (\mathbf{x} - \bar{\mathbf{x}})^{\mathrm{T}} \, \mathbf{P}^{-1} \, (\mathbf{x} - \bar{\mathbf{x}}) \quad , \tag{4}$$

where $\mathbf{P}$ represents the posterior covariance matrix. Note that, instead of the filter residuals, we use the difference between the posterior state $\mathbf{x}$ and prior state $\bar{\mathbf{x}}$ in this case.

In order to define a criterion for the successful detection of a given manoeuvre for the synthetic observations, we first determined the average value $\varepsilon_{\mathrm{avg}}$ and its RMS σ_ε from the observations after the settling phase of the filter but before the manoeuvre, and averaged again over all data sets in a given scenario. For a manoeuvre to count as detected, we require the maximum value $\varepsilon_{\max}$ of the peak to be $5\,\sigma$ above the mean, i.e.,

$$R_\varepsilon = \frac{\varepsilon_{\max} - \varepsilon_{\mathrm{avg}}}{\sigma_\varepsilon} > 5 \quad , \tag{5}$$

and equivalently for ξ.

For this work, we assume that the tracklet-to-object correlation has been successful. This may not always be the case in reality, and the problems of tracklet-to-object matching and manoeuvre detection are closely related (see e.g. [11]). For example, an unusually large "manoeuvre" may in fact be an artifact of a wrong object correlation. Hence, manoeuvre detection may in turn inform tracklet-to-object correlation in some iterative procedure, but a detailed discussion of such an approach is beyond the scope of this paper.

3.2 Conjunction Analysis

Once a manoeuvre is detected, we can determine its epoch by means of the conjunction analysis method described in [5]. For that, we numerically propagate the state estimates at the observation epochs bracketing the manoeuvre forward and backward in time, respectively. We then compute the probability of collision between the forward- and backward-propagated (FWP, BWP) tracks for every step following [12], and find the manoeuvre epoch to be the time of maximum collision probability. Note that we always assume impulsive manoeuvres for this work. Following that, we can determine the $\Delta\mathbf{v}$-components by direct comparison between the FWP and BWP states at the manoeuvre epoch, given that the OD steps have been performed successfully for the orbital stages before and after the manoeuvre.

4 Results

4.1 Results for Synthetic Observations

In order to demonstrate the effect of varying different properties in the synthetic observations, we first created several data sets spanning two days and comprising a total of 100 equally spaced observations each. Unless stated otherwise (as in the last paragraph of Sect. 4.1.3), the modelled manoeuvre takes place exactly after one day, that is, between observations 50 and 51. While this observing cadence is admittedly unrealistic for several reasons (day-night-cycle, object visibility, very limited telescope time per object, etc.), these data sets have been an extremely valuable test bed during the development of the algorithms. Furthermore, we did not want to complicate things unnecessarily as a basic first step, and potentially introduce unwanted artifacts due to a specific pattern of the observation times.

4.1.1 Effect of Manoeuvre Magnitude

We created 10 sets of synthetic observations with different manoeuvre magnitudes ranging from

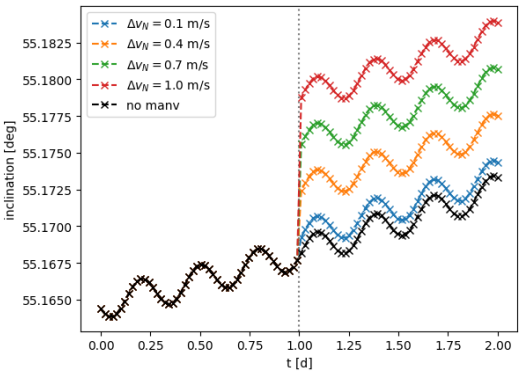

Fig. 1: The effect of several out-of-plane manoeuvres on the inclination. The dotted vertical line represents the manoeuvre epoch.

$0.1\,\mathrm{m\,s^{-1}}$ to $1.0\,\mathrm{m\,s^{-1}}$ in steps of $0.1\,\mathrm{m\,s^{-1}}$, keeping the manoeuvre direction and the noise level in RA and DEC constant. We used a typical value of $2''$ for the noise in both RA and DEC. For the sake of simplicity, we also decided to give the change in velocity only an out-of-plane component, i.e., $\Delta\mathbf{v}_{RTN} = (0, 0, |\Delta\mathbf{v}_{RTN}|)$. Figure 1 shows the effect on the inclination, which is a good quantity to visualize the effect of out-of-plane manoeuvres. Note that, because they only have an out-of-plane component, the manoeuvres are indiscernible when looking at the semi-major axis (not shown here), which is a good quantity to visualize the effect of in-plane manoeuvres. Also note that the model solutions are shown before any noise was added.

The two manoeuvre indicators ε and ξ defined in Sect. 3.1 are shown in Fig. 2 for a subset of the 10 data sets. As expected, it is evident that manoeuvres with larger magnitudes are more readily detected, whereas the smallest manoeuvre ($|\Delta\mathbf{v}_{RTN}| = 0.1\,\mathrm{m\,s^{-1}}$, blue line with diamonds) is not detectable with either indicator. Note the different y-scales and the fact that ξ is noisier than ε. The slightly elevated noise level at the start is caused by the filter still settling in.

Figure 3 shows the significance levels of the detected manoeuvres. As can be seen, the significance levels for both indicators rise slightly steeper than linear with increasing manoeuvre magnitude, but using ε results in much higher levels of significance. All manoeuvres except for the smallest are detected using ε, whereas the two smallest ma-

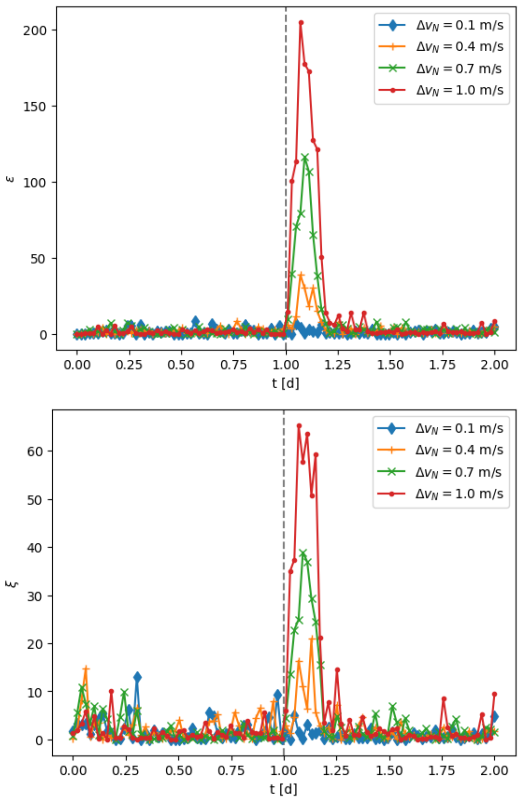

Fig. 2: Squared and normalized residuals in measurement space (ε, upper panel) and in state space (ξ, lower panel) for out-of-plane manoeuvres of different magnitudes.

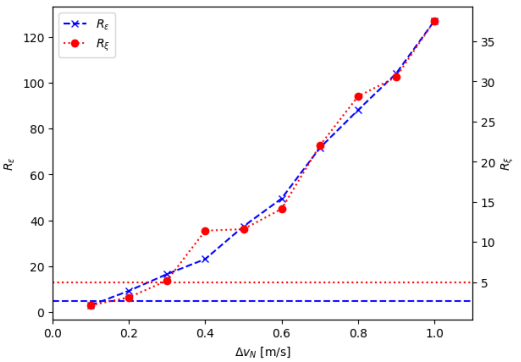

Fig. 3: Significance levels of the detected manoeuvres for ε and ξ as a function of manoeuvre magnitude. The horizontal lines indicate the respective 5-σ levels. Note the different y-scales for R_ε and R_ξ.

noeuvres are missed when using ξ, with the third manoeuvre only being marginally detected.

4.1.2 Effect of Measurement Noise

In order to study the effect of varying measurement noise on the manoeuvre detection efficacy, we created 10 sets of synthetic observations with noise levels ranging from $0.5''$ to $5''$ in steps of $0.5''$, keeping the manoeuvre magnitude fixed at $1\,\mathrm{m\,s^{-1}}$. As before, we only gave the manoeuvres non-zero out-of-plane components. The theoretical effect of such a manoeuvre on the inclination has already been shown in Fig. 1, where the biggest effect shown corresponds to a manoeuvre magnitude of $1\,\mathrm{m\,s^{-1}}$.

Figure 4 shows the manoeuvre indicators for a subset of the 10 data sets. Clearly, and in complete agreement with intuition, manoeuvres are more readily detected when the level of measurement noise is lower. In this case, both indicators facilitate the detection of the manoeuvre for all of the 10 noise levels, although ε does so with much higher significance, as can be seen in Fig. 5.

4.1.3 Effect of Manoeuvre Direction

The third variable whose effect on the detection efficacy we study here is the manoeuvre direction. Assuming that the simulated manoeuvres only ever have tangential and normal components, we define the angle ϕ in the T-N-plane via

$$\Delta\mathbf{v}_{RTN} = (0, v\sin\phi, v\cos\phi) \quad , \qquad (6)$$

where $v = |\Delta\mathbf{v}_{RTN}|$. Thus, $\phi = 0$ corresponds to $\Delta\mathbf{v}_{RTN} = (0, 0, v)$, which is the manoeuvre direction used in the simulations with varying manoeuvre magnitude and/or measurement noise. Here, we created 12 data sets with ϕ ranging from 0 to 330° in steps of 30°. The manoeuvre magnitude and measurement noise in RA and DEC were kept fixed at $1\,\mathrm{m\,s^{-1}}$ and $2''$, respectively.

The effects of these manoeuvres on the inclination and the semi-major axis are shown in Fig. 6. Evidently, when the effect on the inclination is largest, the effect on the semi-major axis is smallest and vice versa. Angle pairs that produce (almost) the same effect as others are plotted as one line only for the sake of clarity.

The detection significance levels show a clear variation with ϕ, and from Fig. 7 it seems that

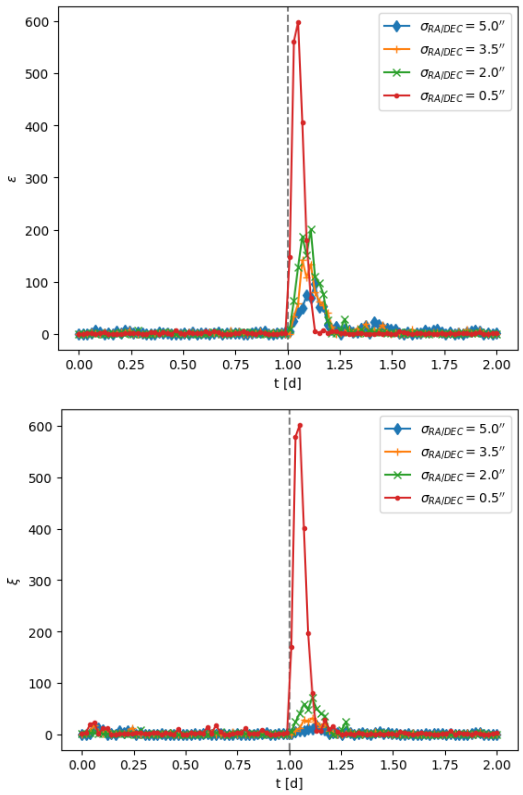

Fig. 4: Squared and normalized residuals in measurement space (ε, upper panel) and in state space (ξ, lower panel) for different levels of measurement noise.

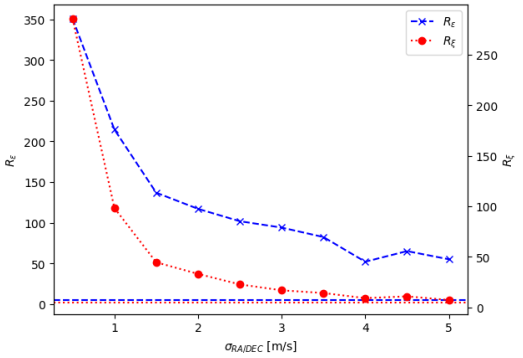

Fig. 5: Significance levels of the detected manoeuvres for ε and ξ as a function of measurement noise. Note the different y-scales for R_ε and R_ξ.

in-plane manoeuvres ($\phi = 90°$ or $\phi = 270°$) are more readily detected than out-of-plane manoeu-

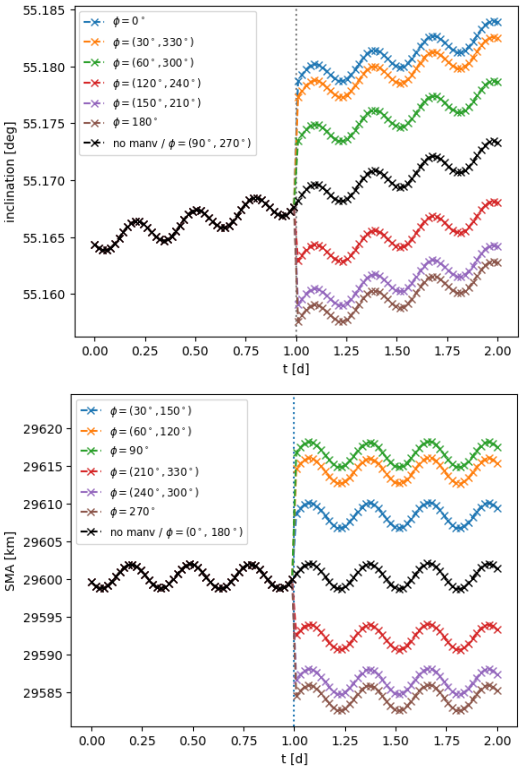

Fig. 6: The effect of manoeuvres in the T-N-plane on inclination (upper panel) and semi-major axis (lower panel).

vres. The effect is much more pronounced for ξ compared to ε. This implies that the direction of a manoeuvre determines which of the two quantities ε and ξ is better suited to be used as the manoeuvre indicator. In-plane manoeuvres are more readily detected via ξ, whereas ε seems to be the better choice for out-of-plane manoeuvres.

In order to verify these findings, we repeated the above experiment using different manoeuvre times, so that the manoeuvres would take place at different orbital phases. Given the orbital period of approximately 845 minutes for Galileo satellites, we divided the orbit into five equal steps of 169 minutes, corresponding to 72° in true anomaly. We found the significance levels to vary in a sinusoidal manner with ϕ in all scenarios. More precisely, for R_ε, both the magnitude and the phase of this variation were found to be consistent, except for some noise. A similar variation with the same phase is also observed for R_ξ, albeit with differences in the

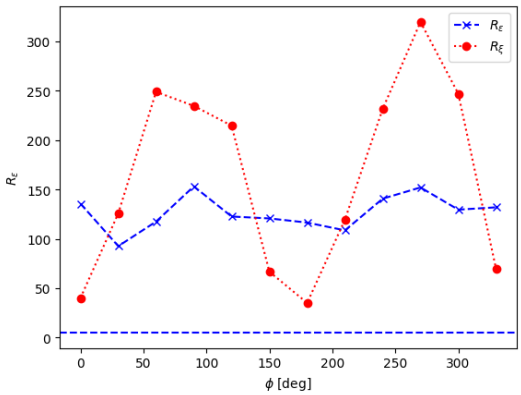

Fig. 7: Significance levels of the detected manoeuvres for ε and ξ as a function of manoeuvre magnitude.

amplitude variations.

4.1.4 Combined Effect of Manoeuvre Magnitude and Measurement Noise

As the significance level of a manoeuvre detection strongly depends on both, manoeuvre magnitude $v = |\Delta\mathbf{v}|$ and measurement noise σ, it is informative to study the combined effect of these variables on the efficacy of the manoeuvre detection algorithm. For this, we created 100 data sets with the values of (v, σ) spanning a two-dimensional grid ($v = 0.1...1.0\,\mathrm{m\,s^{-1}}; \sigma = 0.5...5.0''$). The angle ϕ was fixed at zero. Figure 8 shows the significance levels P_ε and P_ξ as functions of v and σ. As expected, the detection significance drops with increasing measurement noise and with decreasing manoeuvre magnitude.

Another useful quantity to look at is the ratio of the manoeuvre magnitude and measurement noise $q = \frac{v[\mathrm{m\,s^{-1}}]}{\sigma[''] }$. As can be seen in Fig. 9, while the relation between P_ε and q is roughly linear but very noisy, there is a clear power-law relationship between P_ξ and q. Despite the noisiness, we can deduce from Fig. 9 that we can expect to detect manoeuvres using ε as an indicator if $q > 0.07$. Similarly, we determine that we need $q > 0.18$ for the likely detection of a given manoeuvre when using ξ as an indicator. However, note that some manoeuvres may still be detected, even if q is lower than these respective thresholds, which means the quoted minimum values are a conservative estimate. Therefore, the quantity q should be used

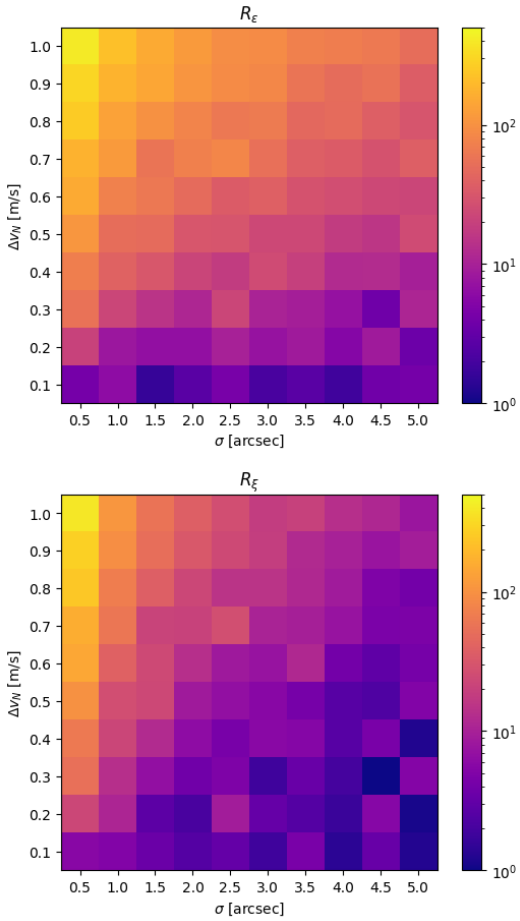

Fig. 8: Significance levels of the detected manoeuvres for ε (upper panel) and ξ (lower panel) as a function of manoeuvre magnitude v and measurement noise σ.

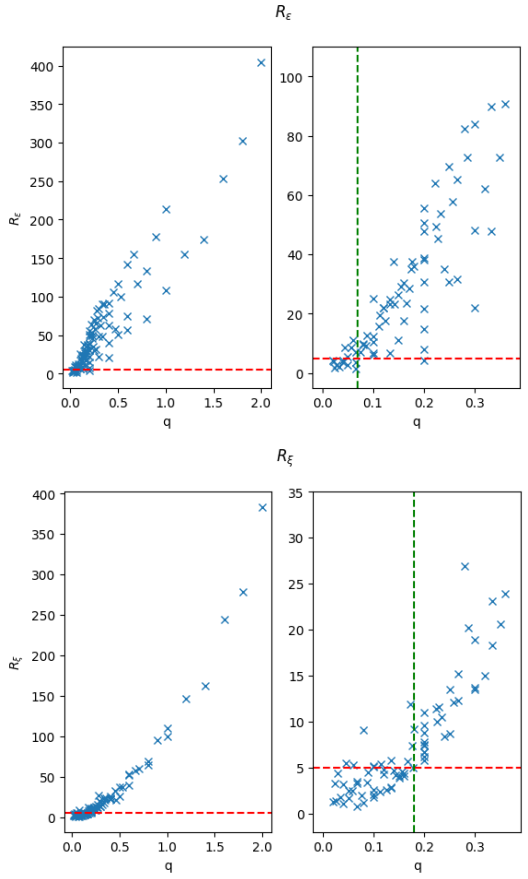

Fig. 9: Significance levels of the detected manoeuvres for ε (upper panels) and ξ (lower panels) as a function of q. The right panels are close-up versions of the lower left corners of the corresponding left panels. The red horizontal dashed lines indicate the 5-σ thresholds, and the green vertical dashed lines indicate the values of q, above which a manoeuvre is likely to be detected.

with caution, although it can serve as a valuable rule of thumb for planning purposes. Note that we repeated this experiment for $\phi = 90°$, and while the exact shape of and scatter in the distribution of R_ε and R_ξ was found to be somewhat different, the overall agreement was good.

4.1.5 Effect of Random Noise

The entire analysis in Section 4.1 should ideally be performed using a Monte Carlo method, because when adding white noise, we are drawing from a Gaussian probability distribution. Hence, every white-noise realization will produce slightly different synthetic observations. Clearly, some realizations of the noise will be more beneficial to detecting a manoeuvre than others. Unfortunately, running these simulations with a significant number of white-noise realizations for every possible combination of manoeuvre magnitude, direction, and noise level, would not have been feasible. However, in order to get a feel for the effect, we created 10 realizations of the same noise level while also keeping all other parameters constant for a small number of scenarios that result in quite different detection significance levels. This crude analysis suggests that

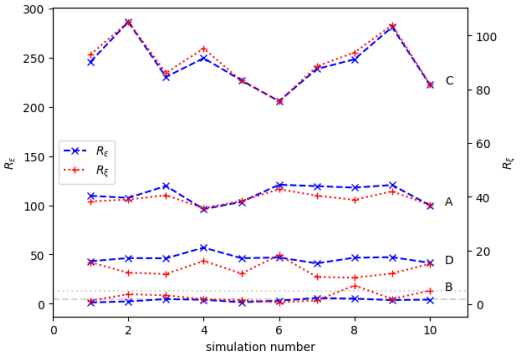

Fig. 10: Significance levels for 10 different white-noise realizations calculated for four different scenarios. The grey horizontal lines indicate the 5-σ thresholds. Note the different y-scales.

the significance levels shown in Figs. 3, 5, 7, 8, and 9 are of the order of 10%. Furthermore, we found the significance levels R_ε and R_ξ to be similarly affected by white noise, in other words, white-noise realizations that have a beneficial/detrimental effect on R_ε will also have a beneficial/detrimental effect on R_ξ. For example, Fig. 10 shows how the detection significance varies for 10 different realizations of measurement noise for four different scenarios (see Table 1).

Table 1: Settings used when creating the synthetic observations shown in Fig. 10.

version	v [m s^{-1}]	ϕ [°]	σ [″]
A	1.0	0	2.0
B	0.1	0	2.0
C	1.0	0	1.0
D	1.0	0	5.0

4.2 Results for SMARTnet Observations

4.2.1 ASTRA-1M

As a real-world example, we analyzed a subset of 292 tracklets containing a total of 1886 individual observations of the geostationary SES ASTRA-1M satellite, taken over five nights in April 2019 with both sensors of the SMART-01-SUTH telescope station in South Africa. Two station keeping manoeuvres happened during this time interval, one North-South (NS) manoeuvre (out-of-plane manoeuvre) and one East-West (EW) manoeuvre (in-plane manoeuvre). The theoretical effect of these manoeuvres on the right ascension and declination is shown in Fig. 11, and Fig. 12 shows the evolution of these quantities together with our measurements, which agree very well with the model. Note that the changes in RA are not visible on this scale.

We passed our observations through the UKF as described in Sect. 3. The filter residuals in measurement space are shown in Fig. 13. Based on observations of GNSS satellites with precisely known orbits, we used a conservative guess of 2″ as the standard value for the measurement noise in both RA and DEC. Before the first manoeuvre, the RMS of the residuals in RA and DEC is 0.50″ and 0.27″, respectively, indicating a good filter performance.

The posterior states of the UKF after every update step are shown in Fig. 14, which also shows the numerically propagated models with and without applying the manoeuvres. As can be seen, the estimated values for the inclination nicely follow the numerical model, and after the NS manoeuvre, which causes a sudden change in the inclination, the filter converges to a good solution again after a short settling phase. On the other hand, the filter estimates for the semi-major axis display significantly more jitter, and the magnitude of this jitter is comparable to the effect of the EW manoeuvre, which explains why the EW manoeuvre is not as easily detected (see below).

The NS manoeuvre is clearly visible in the squared and normalized residuals shown in Fig. 15. As was shown in [4] and [7], the quantity ε is a good indicator for NS manoeuvres, but it is not very sensitive to EW manoeuvres. The EW manoeuvre is, however, visible in the quantity ξ, albeit with a lower significance than some of the other peaks that are not caused by manoeuvres. Evidently, ξ is more severely affected by gaps in the observations as compared to ε. However, the magnitude of the EW manoeuvre is about a factor of 20 smaller than the magnitude of the NS manoeuvre in this particular case. The findings in Sect. 4.1 suggest that such a small manoeuvre magnitude may be towards the lower end of what can be detected with our method. In addition, the EW manoeuvre has a rather long duration of a few hours, so the as-

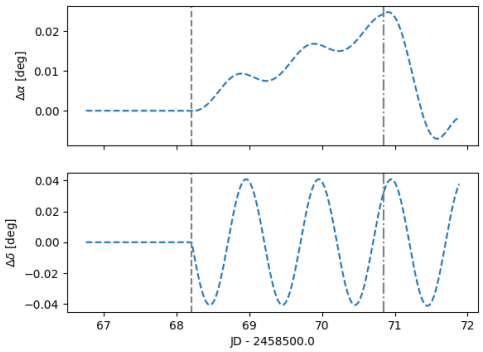

Fig. 11: Effect of the two station keeping manoeuvres on right ascension (upper panel) and declination (lower panel). The vertical grey lines indicate the manoeuvre epochs (NS: dashed, EW: dash-dotted).

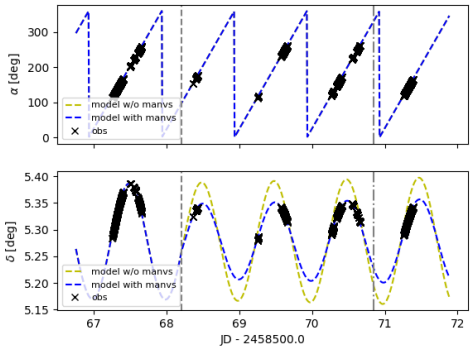

Fig. 12: Evolution of right ascension (upper panel) and declination (lower panel).

sumption of impulsive manoeuvres is violated. Also note that the deviations from the numerical model for the semi-major axis are consistent with the two spurious peaks in the lower panel of Fig. 15 that are not caused by manoeuvres.

For the case of the NS manoeuvre, we applied the conjunction analysis method described in Sect. 3.2. As there were hundreds of observations before and after each manoeuvre, the piece-wise orbit determination produced reliable results, so that we could also get accurate manoeuvre $\Delta\mathbf{v}$-components. Figure 16 shows the physical distance between the forward- and backward-propagated states as well as their collision probability over the time period spanned by the observation epochs bracketing the

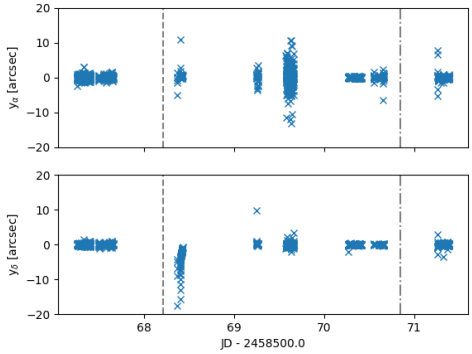

Fig. 13: UKF residuals in right ascension (upper panel) and declination (lower panel).

manoeuvre. As expected, the collision probability reaches a maximum when the distance between the FWP and BWP states is smallest.

As the gap in the observations is longer than 12 hours, there is an ambiguity in the determination of the manoeuvre epoch. Except for a sign flip, the estimated manoeuvre $\Delta\mathbf{v}$-components are nearly identical for these epochs though, and thus, any subsequent orbit determination will not be severely affected if the incorrect peak is selected from Fig. 16. Selecting the correct peak, we were able to determine the manoeuvre epoch to within 7.5 seconds using the maximum of the collision probability. The corresponding estimate of the manoeuvre magnitude was accurate to within $1\,\mathrm{cm\,s^{-1}}$ for the T- and N-components, and to within $7\,\mathrm{cm\,s^{-1}}$ for the radial component. Of special interest for NS manoeuvres is the accuracy in the normal component, which lies well within 1% in this case[2].

We tried the same analysis for the EW manoeuvre, but the results were not satisfactory, with the estimated manoeuvre epoch being off by several hours. Consequently, the estimation process to determine the $\Delta\mathbf{v}$-components could not produce sensible results either.

[2]The R- and T-components of the NS manoeuvre are both close to zero, so quoting the technically large relative errors would be misleading.

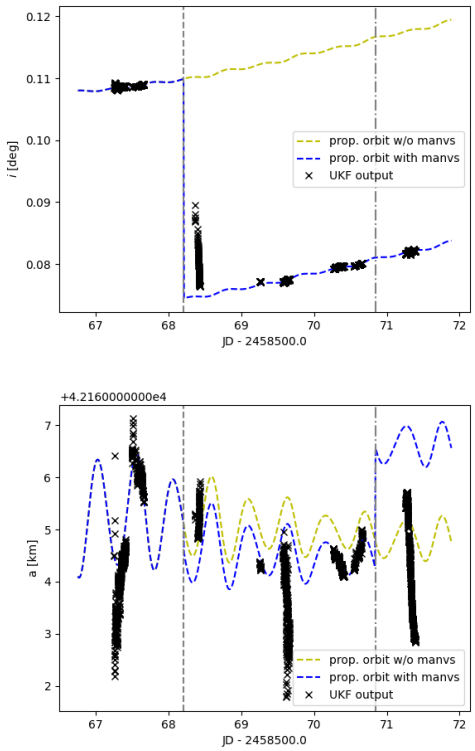

Fig. 14: Evolution of the inclination (upper panel) and the semi-major axis (lower panel) with and without manoeuvres, as well as the filter output.

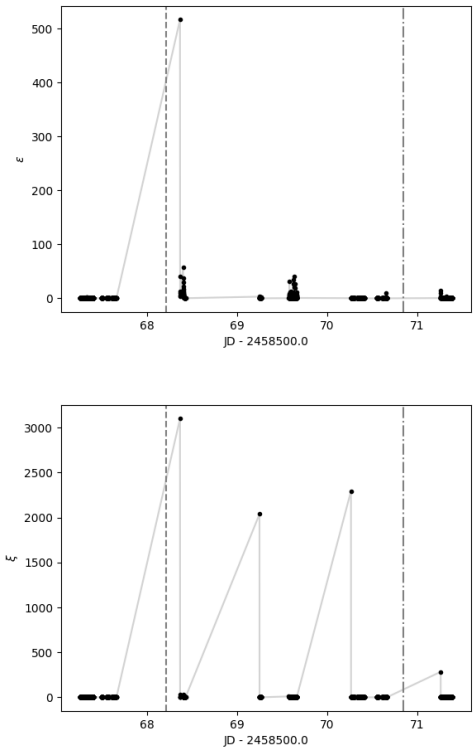

Fig. 15: Squared and normalized residuals in measurement space (upper panel) and in state space (lower panel) for the observations of ASTRA-1M.

4.2.2 Eutelsat Quantum

We also obtained observations of the Eutelsat Quantum satellite, which was launched on 30 July 2021 at 21:00 (UTC) and eventually put into a geostationary orbit at 48° E. Treating this as a target of opportunity to test our manoeuvre detection algorithms, we acquired 80 tracklets comprised of 1031 single-shot exposures with our SMART-01-SUTH telescope station over the first 17 days after the satellite launch. Unfortunately, we do not have the manoeuvre information in this case, so we can only arrive at tentative results.

As before, we employed the UKF using the same standard value of 2″ for the measurement uncertainties in RA and DEC, and detected several significant peaks in the manoeuvre indicators ε and ξ, as can be seen from the upper panels in Figs. 17 and 18. As we do not yet know the minimum significance level required for a peak to be "real",

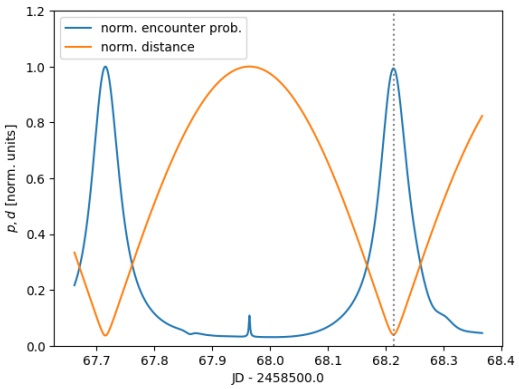

Fig. 16: Encounter probability p and distance d between the forward- and backward-propagated states bracketing the NS manoeuvre. The dotted vertical line indicates the true manoeuvre epoch.

i.e., caused by a manoeuvre, we simply selected the

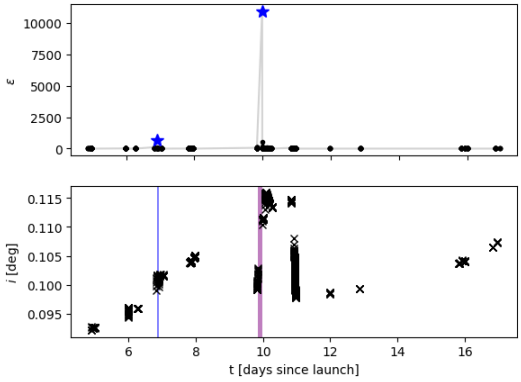

Fig. 17: *Upper panel*: Squared and normalized residuals in measurement space for Eutelsat Quantum. The blue stars mark the manoeuvre epochs after a suspected NS manoeuvre. *Lower panel*: Inclination derived from the UKF output. The shaded areas correspond to the possible time spans during which the suspected manoeuvres could have happened.

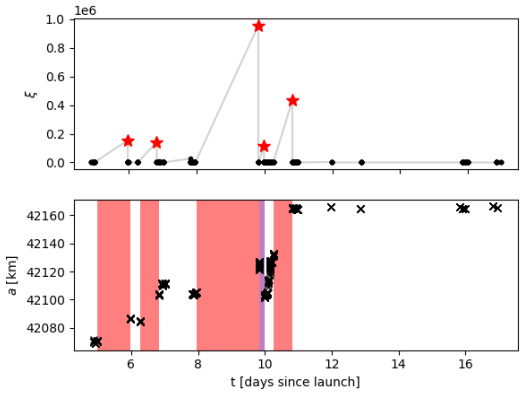

Fig. 18: *Upper panel*: Squared and normalized residuals in state space for Eutelsat Quantum. The red stars mark the manoeuvre epochs after a suspected NS manoeuvre. *Lower panel*: Semi-major axis derived from the UKF output. The shaded areas correspond to the possible time spans during which the suspected manoeuvres could have happened.

most significant ones by hand. These peaks are indicated by star symbols. As there are two significant peaks for ε and five significant peaks for ξ, we speculate that there are two corresponding NS and five corresponding EW manoeuvres. Note that the second marked peak in ε corresponds to the fourth marked peak in ξ. It is conceivable for more than one manoeuvre to occur in a given observation gap, but we would not be able to distinguish this from a single manoeuvre here. Also note that it is equally possible for a peak in the indicators not to correspond to a manoeuvre, as was the case in Sect. 4.2.1.

We would expect to see the manoeuvres in the orbital elements derived from the posterior UKF state estimates. Thus, we plotted the inclination and the semi-major axis in the lower panels of Figs. 17 and 18, respectively. Note that we used purple shading for the peak that shows up in both indicators. Some peaks in the indicators do not seem to coincide with a sudden change in the orbital elements, while others do. For example, there is a sudden change in the inclination for the second suspected NS manoeuvre, and there is also a sudden change in the semi-major axis for the last suspected EW manoeuvre.

5 Discussion and Outlook

We have used our prototype manoeuvre detection algorithm using an UKF to detect manoeuvres successfully in both synthetic and real observations. The synthetic observations have a near-continuous observing pattern and provided valuable insights and often served as a sanity check during the development and testing stages of the algorithm. While this might be over-simplifying things, the synthetic observations analyzed here are based on Galileo orbits, thereby presenting a more challenging scenario as compared to geostationary satellites for several reasons. These include limited object visibility and the fact that the line of sight to the object is not always perpendicular to the object's trajectory. Consequently, the effects of in-plane and out-of-plane manoeuvres on RA and DEC become intertwined.

Our analysis confirms that manoeuvres are more readily detected when their magnitude is larger, and when the level of measurement noise is smaller. By combining those two quantities, we showed that the ratio $q = v/\sigma$ must be above a certain threshold for a manoeuvre to be safely detected. Furthermore, the manoeuvre direction was also shown to have an influence on the significance level of the detection. ε seems to be the better choice for out-of-plane manoeuvres, whereas ξ performs better for

in-plane manoeuvres. The results of Sect. 4.2.1 appear to confirm this.

We found the peaks in the manoeuvre indicators for the near-continuous synthetic observations not to be as sharp as those for real observations. This can be explained by the fact that the orbit has not yet evolved far enough from the pre-manoeuvre orbit at the next observation epoch. This would present a problem for the determination of the manoeuvre epoch with the conjunction analysis method described in Sect. 3.2, as the peak in the indicators is not reached until a few observations after the manoeuvre. However, this observing pattern is completely unrealistic, and the same phenomenon does not occur for the case of realistic observing patterns presented in Sect. 4.2.

The results of Sect. 4.1.3 show that the detection significance depends on the true anomaly of the observation epochs after the manoeuvre. For example, if the first observation after an out-of-plane manoeuvre is taken when the satellite is near the line of nodes between the orbital planes before and after the manoeuvre, the filter residuals (in RA and DEC) will be much smaller as compared to the residuals for an observation taken at a true anomaly that is larger by $\pi/2$. A further in-depth analysis (as part of the Monte Carlo simulations mentioned in Sect. 4.1.5) is planned to investigate this effect.

It is noted that the synthetic observations were based on numerically propagated states of an initial state vector, and that the propagation is the same as the one used in the state transition function of the UKF. Therefore, the noise in ε and ξ is only due to the simulated noise in the synthetic observations and the fluctuations of the filter output around the true orbit. However, in the case of real observations, there will be additional noise in the manoeuvre indicators, especially for longer gaps in the data, because the numerical propagation cannot perfectly predict the evolution of a real satellite orbit in the presence of perturbations. Thus, even if no manoeuvre has happened, there will be a discrepancy between the observed states and the predicted states that is growing with longer prediction times.

To close the gap between the near-continuous synthetic observations and real observations, we are planning to repeat the analysis in Sect. 4.1 with more realistic observing patterns, including effects like the grouping of observations in series of $\sim$7 single-shot exposures, telescope station downtime due to bad weather and/or arbitrary technical problems, and the diurnal cycle. Of course, unless this analysis was performed for a geostationary object, object visibility will also be a major factor. We also plan to expand this analysis to include synthetic observations from multiple observing sites and to study the effect of observing at different points in the orbit after a manoeuvre on the detection significance. This, in turn, should give us valuable feedback for the optimization of the observation planning process.

We also applied our methodology to a subset of SMARTnet observations of the geostationary SES ASTRA-1M satellite. While the larger NS manoeuvre was readily detected, the significance of the peak caused by the much smaller EW manoeuvre was much lower, being deeply buried in the noise. Moving forward, we determined the epoch of the NS manoeuvre to within a few seconds and the $\Delta\mathbf{v}$-components to the cm/s-level. This level of accuracy is very encouraging, although a limiting factor is the sparseness of observations. The observations of ASTRA-1M were taken during a special observational campaign, but in most other cases we do not have the same amount of data available. More tests are needed to determine the minimum number and density of observations needed to detect and characterize manoeuvres, with the latter goal being more demanding as it can easily become hampered if the piece-wise OD does not produce accurate results.

A preliminary analysis using observations of the Eutelsat Quantum satellite also produced tentative manoeuvre detections. For lack of manoeuvre data, we cannot verify if the suspected manoeuvres really happened at this stage, or if there are some spurious peaks caused, for example, by the filter not having settled on the true orbit state beforehand. We also cannot rule out that we missed some manoeuvres due to sparse observations or for any other reason. Note that we tried to perform a piece-wise OD but did not obtain satisfactory results owing to the limited number of observations between the suspected manoeuvres. Therefore, we did not attempt to estimate the manoeuvre epochs and $\Delta\mathbf{v}$-components here. Nevertheless, this analysis demonstrates again the potential to detect manoeuvres for geostationary satellites, including manoeuvres during the launch and early-orbit phase.

After performing a number of manoeuvres during the first few days, it looks like the satellite has reached its nominal position about 10.5 days after launch. These findings do sound completely reasonable for a satellite that is still being steered to its final destination.

One limitation of our conjunction analysis method is the need to have a sufficient number of observations in-between manoeuvres, so that a piece-wise OD process can produce reliable orbits. Note, however, that the detection method will still work, so that an automated planning tool will eventually be able to increase the observing cadence of an object whenever it is found to have executed a manoeuvre.

Furthermore, while the results obtained with our prototype algorithms are promising, it is necessary to make the processing more robust. For example, we found that a handful of "bad" tracklets can cause the UKF to diverge from the true orbit, resulting in spurious peaks in the manoeuvre indicators. These can potentially mask peaks that are actually caused by manoeuvres.

In order to refine the manoeuvre estimation, it may be beneficial to include the manoeuvre epoch and $\Delta\mathbf{v}$-components as free parameters in a batch least-squares OD step, using the values determined with the method described in this work as starting values. In the same way, extended manoeuvres could be accounted for by also including the thruster-firing duration.

Acknowledgements

We would like to thank SES S.A. for kindly providing us with the relevant manoeuvre information for their ASTRA-1M satellite.

List of Abbreviations

BWP	Backward-Propagated
DEC	Declination
EKF	Extended Kalman Filter
EW	East-West
FWP	Forward-Propagated
OD	Orbit Determination
NS	North-South
RA	Right Ascension
UKF	Unscented Kalman Filter

References

[1] T. Kelecy, D. Hall, K. Hamada, M. D. Stocker, Satellite Maneuver Detection Using Two-Line Element (TLE) Data, Advanced Maui Optical and Space Surveillance (AMOS) Technologies Conference, Maui, Hawaii, USA, 2007, 12-15 September.

[2] W. D. Song, R. L. Wang, J. Wang, A simple and valid analysis method for orbit anomaly detection, *Advances in Space Research*, 49 (2012) 386-391.

[3] S. Lemmens, H. Krag, Two-Line-Elements-Based Maneuver Detection Methods for Satellites in Low Earth Orbit, *Journal of Guidance, Control, and Dynamics*, 37 (2014) 860-868.

[4] A. Zollo, Satellite maneuver detection and estimation using optical measurements, MSc thesis, Institut Supérieur de l'Aéronautique et de l'Espace and Deutsches Zentrum für Luft- und Raumfahrt (2020).

[5] J. Herzog, H. Fiedler, T. Schildknecht, Using Conjunction Analysis Methods for Manoeuvre Detection, 7th European Conference on Space Debris, Darmstadt, Germany, 2017, 18-21 April.

[6] Y. Jiang, H. Yang, H. Baoyin, P. Ma, Extended Kalman Filter with Input Detection and Estimation for Tracking Manoeuvring Satellites, *The Journal of Navigation*, 72 (2019) 628-648.

[7] C. Bergmann, A. Zollo, J. Herzog, H. Fiedler, T. Schildknecht, Integrated Manoeuvre Detection and Estimation Using Nonlinear Kalman Filters During Orbit Determination of Satellites, 8th European Conference on Space Debris, Darmstadt, Germany, 2021, 20 – 23 April.

[8] H. Fiedler, J. Herzog, M. Ploner, et al., SMARTnet™– First Results of the Telescope Network, 7th European Conference on Space Debris, Darmstadt, Germany, 2017, 18 – 21 April.

[9] T. Flohrer, T. Schildknecht, C. Früh, R. Musci, M. Ploner, Optical Observations at the Zimmerwald Observatory, 58th International Astronautical Congress, Hyderabad, India, 2007, 24 – 28 September.

[10] Y. Bar-Shalom, L. Xiao-Rong, T. Kirubarajan, Estimation with applications to tracking and navigation, first ed., Wiley, Hoboken, 2001.

[11] R. Serra, C. Yanez, C. Früh, Tracklet-to-orbit association for maneuvering space objects using optimal control theory, *Acta Astronautica*, 181 (2021) 271-281.

[12] S. Alfano, Relating Position Uncertainty to Maximum Conjunction Probability, *The Journal of the Astronautical Sciences*, 53 (2005) 193-205.